

Collisions enhance tracer diffusivity in an active Janus bath

Maximilian R. Bailey,¹ Dmitry A. Fedosov,² Federico Paratore,¹ Fabio Grillo,¹ Gerhard Gompper,² and Lucio Isa^{1,*}

¹Laboratory for Soft Materials and Interfaces, Department of Materials,
ETH Zürich, Vladimir-Prelog-Weg 5, 8093 Zürich, Switzerland

²Theoretical Physics of Living Matter, Institute of Biological Information Processing and
Institute for Advanced Simulation, Forschungszentrum Jülich, 52425 Jülich, Germany

(Dated: November 7, 2023)

The generation of fluid flows by autophoretic microswimmers has been proposed as a mechanism to enhance mass transport at the micro- and nanoscale. Here, we experimentally investigate the ability of model “active baths” of photocatalytic silica-titania Janus microspheres to enhance the diffusivity of tracer particles at different microswimmer densities excluding collective effects. Inspired by the similarities between our experimental findings and previous results for biological microorganisms, we also model our Janus microswimmers using a general squirmer framework. The numerical simulations faithfully capture our observations, offer an insight into the microscopic mechanism underpinning tracer transport, and allow us to expand the parameter space beyond our experimental system. We find strong evidence for a collision-based mechanism for increased tracer diffusivity, which leads to the identification of an operating window for enhanced tracer transport by chemical microswimmers based on dimensionless scaling arguments.

The ability of active matter to transduce available energy into directed motion has inspired research across various disciplines [1, 2]. Amongst the systems studied at the micron-scale, where Brownian fluctuations and viscous forces are significant [3], the “autophoretic” motion of chemical microswimmers has been proposed to induce micro-mixing in fluids [4, 5], with potential applications ranging from environmental remediation [6] to synthetic chemistry [7]. While biological microswimmers have been shown to enhance the diffusivity of passive tracers [8–14], analogous systematic studies of this effect are lacking for synthetic, catalytic microswimmers [15], except for systems propelled by bubble generation [16, 17]. As most synthetic and biological active matter systems do not involve bubble propulsion, an opportunity arises to address this open question with model active colloids.

Here, we investigate the mixing properties of a widely studied synthetic active matter model system consisting of a suspension of photocatalytically active Janus particles with a titania cap under UV illumination. We overcome the limited scale of conventional Janus particle fabrication techniques via “Toposelective Nanoparticle Attachment” (TNA), which exploits an emulsion template and multi-functional polymers to facilitate the selective binding of a broad range of nanoparticles, including the photocatalytic titania nanoparticles used in this study, onto silica particle supports [18, 19]. While experimentally probing the mechanisms leading to the enhanced transport of passive tracers, we observe unexpected parallels between their dynamics in active baths of our synthetic active colloids and previous findings for biological microswimmers, despite their vastly different underlying propulsion schemes. Employing a simple scaling argument, we attribute the increased diffusivity of the colloidal tracers to a collision-based interaction with the Janus microswimmers. We then use a coarse-grained hydrodynamic swimmer model - which generates a force dipole and source dipole in the far-field - to

capture the generic aspects of tracer mixing [20, 21]. Finding good agreement between numerical simulations and experiments, we proceed to study the mixing properties of our hydrodynamic “squirmers” under conditions beyond those experimentally achievable, and highlight key considerations for the realisation of the promise of catalytic “micro-stirrers”.

Specifically, our microswimmers are spherical SiO_2 colloids (diameter $d_S = 2.16\mu\text{m}$) half-decorated with photocatalytic TiO_2 nanoparticles, as described in detail in Refs. [18, 19]. Under UV illumination, the particles asymmetrically degrade H_2O_2 (fuel) and thus establish local chemical gradients, leading to self-propulsion by autophoresis [22–25]. The density mismatch of the particles, coupled with the experimental conditions used (see Supporting Information, Materials & Methods) minimises their out-of-plane motion [26, 27] and ensures that particles move in 2D (xy plane). Under these conditions, we systematically study the behavior of the microswimmers as their effective area fraction ($\Phi = N_p A_p / A_T$, where N_p is the number of microswimmers, $A_p = \pi d_S^2 / 4$, and A_T is the area of the system) is varied. In agreement with previous reports for both synthetic and biological systems [28–36], we observe the formation of “dynamic clusters” above a threshold swimmer density, (see Supporting Information, Figure S1, and compare Videos S1 and S2). The emergence of collective behaviours, although of significant fundamental interest, not only complicates the analysis of the mixing properties of microswimmers, but also likely hinders their overall mixing efficiency [37], as we outline below. We therefore determine the limiting area fraction of microswimmers before the onset of clustering events using the methodology outlined by Theurkauff et al (see Supporting Information, Figure S1a [28]). In agreement with their findings, we determine an onset of clustering at $\Phi \approx 0.05$ (see Supporting Information, Figure S1c), which we thus set as the upper bound for our experiments to focus on single-particle effects. Similar to the seminal work by Wu and Libchaber on the mixing properties of bacterial baths [8], the velocity distribution of our synthetic “free” particles obeys Maxwell’s statistics, however, in its 2D form as particle motion is confined above the substrate:

* E-mail: lucio.isa@mat.ethz.ch

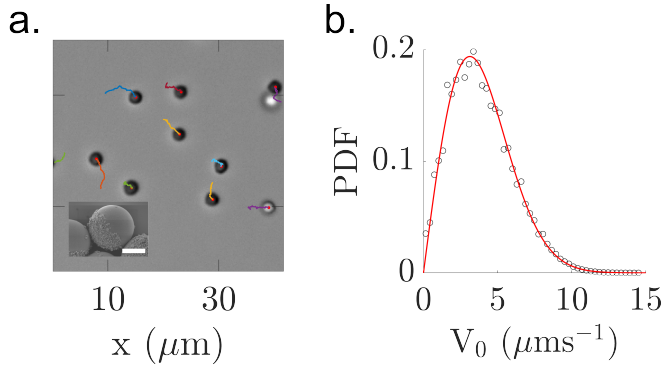


Figure 1. Janus microswimmer 2D motion above a substrate in the absence of clustering. a. Micrograph of “free” particles at low area fraction $\Phi = 0.02$ (1s trajectory). Inset: HR-SEM image of the studied Janus particles. Scale bar represents $1 \mu\text{m}$. b. Distribution of the free microswimmer in-plane velocities measured over 40000 trajectories.

$P(v_0) = \frac{v_0}{v_M^2} \exp(-\frac{v_0^2}{2v_M^2})$, where v_M is the modal velocity. Under the experimental conditions used, our active colloids have a modal velocity $v_M \approx 3.1 \mu\text{ms}^{-1}$ (see Figure 1b).

Following previous work on biological microswimmers, we study the effect of microswimmers on the dynamics of micron-sized tracers (diameter $d_T = 1.70 \mu\text{m}$) [8–10, 12–15]. We find that the tracers display extensive displacements when a microswimmer passes in their vicinity (Figure 2a, Supporting Information Video S3) - which we henceforth refer to as “jumps”. We stress that these enhancements in the motion of the tracers are distinct to previous studies on “colloidal transport”, where the microswimmer actively transports the tracer by a “pick-up and place” type mechanism [38–40] (also see Supporting Information Figure S2 on the over-weighted effect such transported tracers can have on the ensemble mean-squared-displacement (EMSD)). By simple scaling arguments, we now demonstrate that these “jumps” are indeed likely caused by collision events between the tracers and the microswimmers [14].

We start by assuming that the tracers and swimmers are equidistantly distributed. If the translational and rotational diffusion of the swimmers are negligible, the MSD of N swimmers moving with speed v_0 at time τ can be approximated as $\langle \Delta \mathbf{r}^2(\tau) \rangle \sim N_p v_0^2 \tau^2$ at short times [41]. Thus, the time taken for a swimmer to (on average) travel the inter-tracer distance and collide with the tracers can be approximated as $\hat{\tau}_c \sim \frac{\sqrt{A_T}}{v_0 \sqrt{N_p N_{trac}}}$, where N_{trac} is the number of tracer particles (see Supporting Information, Materials and Methods). By plotting the kurtosis γ of tracer displacements for different lag times $\Delta\tau$ and fitting a smoothing curve [42], we observe a Pearson’s correlation coefficient $R = 0.8$ between the scaling time $\hat{\tau}_c$ for collisions estimated by our argumentation, and the experimentally determined lag time $\tau_{\gamma=\text{argmax}_\tau(\gamma)}$ at which the maximum in the kurtosis of the tracer displacements $\gamma(\Delta\tau)$ occurs (see Figure 2b, inset).

$\gamma(\Delta\tau)$ is a measure of non-Gaussianity ($\gamma > 0$ corresponding to heavy tails, and $\gamma = 0$ to Gaussian distributions), and

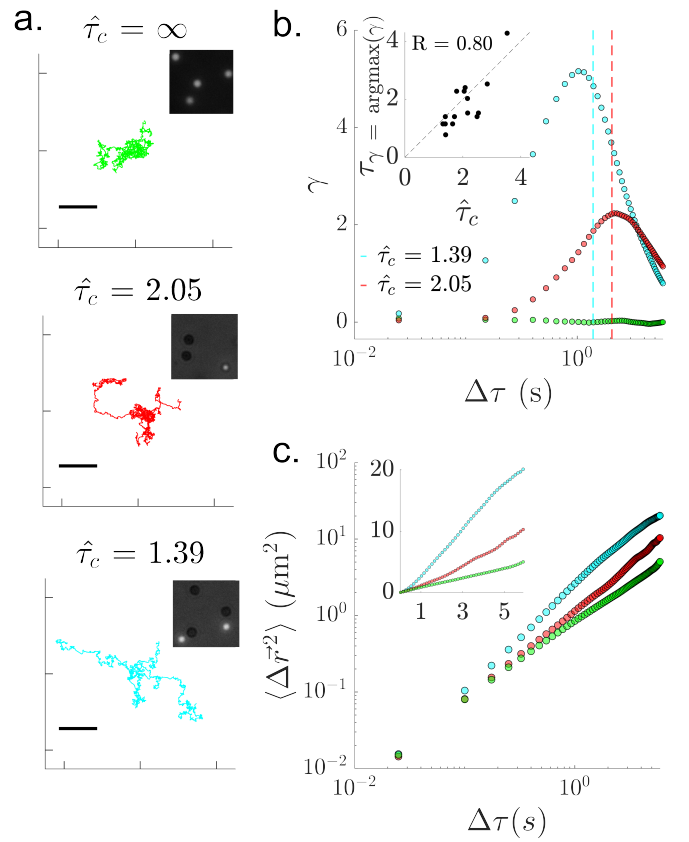


Figure 2. Emergence of large displacements in the trajectories of tracers with the introduction of microswimmers. a. Tracer trajectories for 3 different experimental cases corresponding to various $\hat{\tau}_c$. Scale bars represent $5 \mu\text{m}$. Insets are representative snapshots of the experimental system (bright tracers and dark microswimmers, $16.25 \times 16.25 \mu\text{m}$). b. Evolution of the kurtosis γ of the distribution of displacements with lag time $\Delta\tau$ for the 3 experimental conditions depicted in a. Each data-set contains at least 23 trajectories. The dashed lines indicate $\hat{\tau}_c$ for the given experimental conditions. Inset: Correlation between the estimated collision time $\hat{\tau}_c$ and the experimentally observed lag time at which the kurtosis is maximum ($\tau_{\gamma=\text{argmax}_\tau(\gamma)}$ - see Supporting Information Figure S3). c. Ensemble mean-squared-displacement (EMSD) of the 3 experimental systems depicted in a.

can be expected to capture the presence of tracer jumps. In previous theoretical and experimental work on biological systems [12, 43], the presence of extended tracer displacements upon near-field interactions with the microorganisms was referred to as “entrainment”, arising from no-slip surface interactions and enhancing tracer diffusivity [43–45]. In our synthetic analogues, tracers in active baths with low $\hat{\tau}_c$ also exhibit a larger MSD and thus an increased diffusion coefficient (see Figure 2c). However, we expect that our Janus particles have a diffusiphoretic surface slip velocity [46], precluding the mechanism of entrainment [45].

Further evidence for the enhancement in tracer diffusivity as a result of tracer jumps is presented in Figure 3 (top row). Following Jeanneret et al., we distinguish between standard diffusive motion during a fixed time and jumps, using the autocorrelation of subsequent displacements [12]. Although the

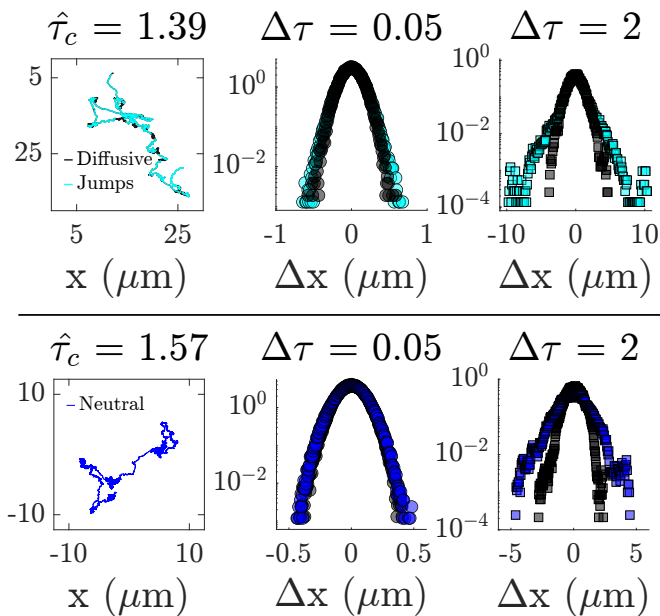


Figure 3. Influence of the jumps on the tracer distribution of displacements at different lag times $\Delta\tau$. Top row: Tracer trajectory in a microswimmer bath. The non-Gaussian, exponential tails in the distribution of displacements becomes prominent at longer lag-times. We note that these tails are not observed for “passive” microswimmers (see Supporting Information, Figure S4). Bottom row: Our numerical neutral squirmer model maps qualitatively well onto the experimental findings, with the presence of jumps at longer $\Delta\tau$ seen in the tails of the distribution of displacements (blue for tracers in the presence of neutral squirmers, black for the passive case).

significantly lower speeds of the studied synthetic microswimmers reduces the effective size of the tracer jumps, it is clear that long-time exponential tails emerge in the distribution of tracer displacements when jumps are included, replicating the findings for microalgae [12]. This qualitative agreement was not expected *a-priori*, but further motivates our modelling of the active colloids as squirmers.

The squirmer model [20], first proposed for microorganisms [47, 48], is frequently invoked to describe the flow fields surrounding chemical Janus microswimmers [21, 27, 49], and generates flows which are consistent with a coarse-grained framework incorporating hydrodynamic effects in the far field via a multipole expansion, together with appropriate near-field fluid flows. We note that a more complete description of chemically active colloids requires the analysis of the phoretic flows resulting from the chemical gradients produced by the microswimmers [50, 51] (see Supporting Information, Figure S5). Still, a complete description of the phoretic and osmotic flows requires the relevant mobility parameters - reducing generalisability to other mixing systems. For a coarse-grained model to describe the mixing properties of our microswimmers, we therefore neglect the phoretic contribution to tracer displacements, following Ref. [52] (also see Supporting Information, Figure S6). In particular, we model our synthetic microswimmers as neutral squirmers (squirmer parameter $\beta = 0$ - see Supporting Information, Materials and

Methods), informed by previous work on catalytic Janus systems [53]. The neutral squirmer model furthermore agrees with the absence of transport behaviours associated with flow vortices [54], the dominant contribution of tracer “jumps” to their diffusivity, and the absence of long-range flow effects [43]. Fluid flow is modelled using dissipative particle dynamics (DPD), a mesoscopic hydrodynamics simulation technique [55, 56]. Both passive and active colloids are represented by a triangulated network of particles placed homogeneously on a spherical surface to ensure a near-rigid shape (see Supporting Information, Materials and Methods). Propulsion is modelled by imposing a slip velocity at the surface of the active particles. For passive particles, no-slip boundary conditions (BCs) are imposed. The simulation domain corresponds to $34 \times 34 \times 6.8 \mu\text{m}$ with periodic BCs in the xy plane, and walls at $z = 0$ and $z = 6.8 \mu\text{m}$. The diameter d_{Sq} of the squirmers is taken to be $2.16 \mu\text{m}$, as in experiments. Both passive and active particles are confined within a layer of $2.45 \mu\text{m}$ at the lower wall with no-slip BCs, to mimic the quasi 2D setup in the experiments. The wall at $z = 6.8 \mu\text{m}$ assumes slip BCs, to better capture experimental conditions. The area fraction of active particles corresponds to $\Phi = 0.05$, identified as the onset of clustering in both experiments and simulations. We underline that our simulation of squirmers with a surface velocity precludes tracer entrainment, which requires a no-slip microswimmer surface [45].

We find that the dynamics of our simulated “tracer” particles in the presence of neutral squirmers are very similar to our experimental findings at similar velocities. Specifically, we identify the presence of “jumps” in the tracer trajectories, which emerge at longer lag times in the distribution of tracer displacements (see Figure 3, bottom row). We therefore proceed to a more quantitative characterisation of the mixing efficiencies of different squirmers, not only for neutral squirmers ($\beta = 0$), but also for pullers ($\beta = 5$), and pushers ($\beta = -5$). As a control, we also study the dynamics of tracer particles in the presence of particles that do not swim (i.e. passive particles). We observe that pushers are significantly superior mixers to other squirmer types in our experimental conditions, as reflected in the EMSD of the tracers (Figure 4a). In fact, we determine a linear trend in D_{eff}/D_0 with $\langle V_0 \rangle$ (Figure 4b), as expected for a predominantly collision-based mechanism for mixing. The superior mixing performance of pushers is attributed to their higher in-plane swimming speeds, which results from the preferential alignment of their swimming axis *parallel* to the substrate, whereas pullers are often oriented perpendicular to the surface (see Figure 4c and inset). As an aside, we note the similarity in the distribution of swimming speeds of our synthetic microswimmers and the neutral squirmers (compare Figures 1b and 4c), underlining the role of orientation with respect to the substrate.

The tracers’ diffusivity enhancement D_{eff}/D_0 also scales approximately linearly with their size in the resolution of our DPD simulations (for a given squirmer velocity - see Figure 4d), indicating the robustness of the “collision” mechanism to not only particle speed but also to the size of the tracers. We thus hypothesise that the mixing capacity of microswimmers is limited by the relative size and frequency of the imparted

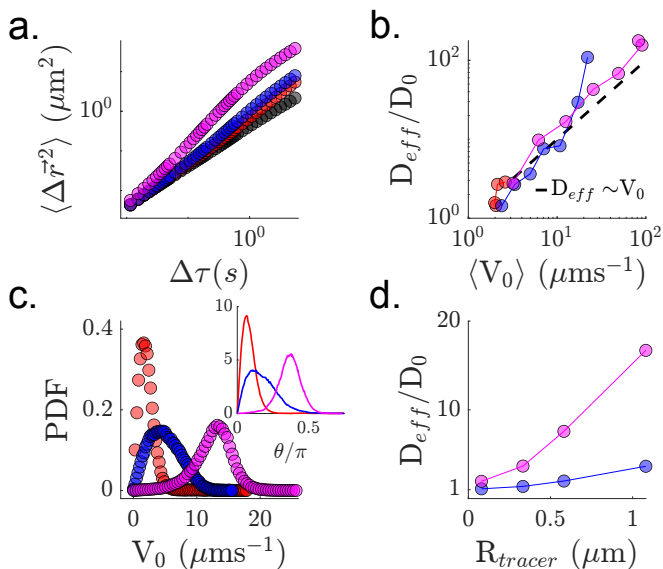


Figure 4. Dynamics of simulated active and tracer particles (black for passive particles, red for pullers, blue for neutrals, and magenta for pushers.) a. Mean-squared displacements of tracers for different squirmer types for velocities approximating experimental values. b. Scaling of normalised tracer diffusion D_{eff}/D_0 with the swimming velocity V_0 of the squirmers. c. Distributions of squirmer in-plane (2D) velocities for fixed squirmer strengths (all types would have the same swimming velocity under unbounded conditions). Inset: Orientation distributions of active and tracer particles with respect to the z axis (i.e. perpendicular to the wall). d. D_{eff}/D_0 for different sizes of passive particles.

“jumps” via collisions compared to the underlying diffusivity of the component to be mixed (i.e. $l_j \gg \sqrt{D_0\tau_c}$ for enhanced mixing, where l_j is the jump length after a collision occurring with frequency $1/\tau_c$). This mirrors the experimental findings using 230 nm nanoparticle tracers where no enhancement in D_{eff} over D_0 was observed (see Supporting Information Figures S7-8), suggesting the unsuitability of this type of microswimmer systems to mix e.g. species with very high diffusion coefficients.

Despite the best laid schemes for microswimmers and mixing, there are still significant hurdles to the “micro-stirrer” concept. This can perhaps be simply illustrated by taking a leaf from Purcell [57], and evaluating the relevant dimensionless numbers involved in enhanced transport for chemical microswimmers. Presuming low Reynolds number conditions $Re = vl/\nu \ll 1$, where ν is the kinematic viscosity and vl relates to the fluid flow at a characteristic length-scale l , for microswimmers swimming in bulk with velocity v (i.e. motion in the viscous regime and ignoring substrate effects), the first relevant ratio is the Péclet “transport” number, $Pe_T = vl/D$ - where D is the translational diffusion coefficient of the transported species. If $Pe_T \ll 1$, the microswimmer is essentially static with respect to the transported species, and we do not expect any diffusivity enhancement. Considering the special case of “chemistry-on-the-fly”, where molecules are “mixed” to enhance the chemical reaction rate [4, 5, 7], $Pe_T \rightarrow 0$ for most experimental systems.

However, Pe_T can be increased by scaling the particle size and speed appropriately (e.g. $d_S \sim 10^2 \mu\text{m}$ moving at some d_S per second). In this case, and staying on the “chemistry-on-the-fly” approach (while ignoring phoretic effects [49]), we can then evaluate the Damköhler Da and Sherwood Sh numbers. $Da = \kappa l/D$ details the balance between the reaction rate κ and the (diffusive) mass transfer process. Notably, the classical continuum phoretic framework to describe chemical microswimmer motion presumes reaction-rate limited kinetics, i.e. $Da \rightarrow 0$ [50, 58–60], with finite values of Da leading to decreasing microswimmer speeds [49] - calling into question the goal of overcoming mass-transfer limitations in reactions using microswimmer motility [4, 5, 7]. Nevertheless, assuming transport-limited reactions, we examine the Sherwood number for mass transfer to a sphere in Stokes flow, $Sh = 2 + 0.991Re^{1/3}Sc^{1/3}$ [61, 62], where $Sc = \nu/D$ is the Schmidt number (the ratio of momentum to mass diffusivity), the first term is for the asymptotic limit of molecular diffusivity, and $0.991Re^{1/3}Sc^{1/3}$ is the advective contribution to mass-transport [62]. In creeping flow, we thus expect the enhancement in mass transfer from fluid advection to be small even when $Pe_T > 1$ for most physical parameters. In highly viscous reactor settings, the micro-stirrer strategy could be effective for e.g. macromolecules with a low diffusivity (assuming the microswimmers do not slow down), however, we underline the poor scaling with the exponent $1/3$.

Basic dimensionless arguments based on convection-reaction-diffusion theory [63] thus provide some additional insight into the challenges of using autophoretic microswimmers as micro-stirrers, besides the limitations posed by neglected effects such as clustering. Still, it is worth noting that collective behaviours could also enhance fluid intermixing and thereby improve reaction-diffusion limitations [64], while appropriate material selection can modify generated flow fields [65, 66] and thereby prevent undesirable aggregation phenomena (i.e. for pushers [36, 67]). Other promising avenues to increase microswimmer mixing could be achieved via modifying their shape away from classical spheres [68], or exploiting bubble generation [69]. Our results therefore underline the need for a more considered approach to the design of synthetic microswimmers to enhance micro- and nanoscale mass transport, and provide evidence that deviations from model (spherical) swimmers may be required for such applications.

Acknowledgements

The authors thank M. Popescu and V. Niggel for helpful discussions on theory and experiment respectively. The authors also thank S. Vasudevan for his assistance with the performed DDM analysis. The authors gratefully acknowledge computing time on the supercomputer JURECA [70] at Forschungszentrum Jülich under grant no. actsys.

Author Contribution Statement

Author contributions are defined based on the CRediT (Contributor Roles Taxonomy). Conceptualisation: M.R.B., D.A.F., F.P., F.G., G.G., L.I. Funding acquisition: L.I. Investigation and analysis: M.R.B., D.A.F. Methodology: M.R.B., D.A.F., F.P. Supervision: L.I. Visualisation and writing: M.R.B., D.A.F., F.P., F.G., G.G., L.I.

- [1] S. Ramaswamy, *Annual Review of Condensed Matter Physics* **1**, 323 (2010).
- [2] G. Gompper, R. G. Winkler, T. Speck, A. Solon, C. Nardini, F. Peruani, H. Löwen, R. Golestanian, U. B. Kaupp, *et al.*, *Journal of Physics: Condensed Matter* **32**, 193001 (2020).
- [3] C. Bechinger, R. Di Leonardo, H. Löwen, C. Reichhardt, G. Volpe, and G. Volpe, *Reviews of Modern Physics* **88**, 045006 (2016).
- [4] E. Karshalev, B. Esteban-Fernández De Ávila, and J. Wang, *Journal of the American Chemical Society* **140**, 3810 (2018).
- [5] B. Dai, Y. Zhou, X. Xiao, Y. Chen, J. Guo, C. Gao, Y. Xie, and J. Chen, *Advanced Science* **9** (2022).
- [6] L. Wang, A. Kaeppeler, D. Fischer, and J. Simmchen, *ACS Applied Materials and Interfaces* **11**, 32937 (2019).
- [7] M. Wittmann, S. Heckel, F. Wurl, Z. Xiao, T. Gemming, T. Strassner, and J. Simmchen, *Chemical Communications* **58**, 4052 (2022).
- [8] X. L. Wu and A. Libchaber, *Physical Review Letters* **84**, 3017 (2000).
- [9] K. C. Leptos, J. S. Guasto, J. P. Gollub, A. I. Pesci, and R. E. Goldstein, *Physical Review Letters* **103**, 1 (2009).
- [10] C. Valeriani, M. Li, J. Novosel, J. Arlt, and D. Marenduzzo, *Soft Matter* **7**, 5228 (2011).
- [11] L. G. Wilson, V. A. Martinez, J. Schwarz-Linek, J. Tailleur, G. Bryant, P. N. Pusey, and W. C. Poon, *Physical Review Letters* **106**, 7 (2011).
- [12] R. Jeanneret, D. O. Pushkin, V. Kantsler, and M. Polin, *Nature Communications* **7**, 1 (2016).
- [13] X. Zhao, K. K. Dey, S. Jeganathan, P. J. Butler, U. M. Córdoba-Figueroa, and A. Sen, *Nano Letters* **17**, 4807 (2017).
- [14] A. Lagarde, N. Dagès, T. Nemoto, V. Démery, D. Bartolo, and T. Gibaud, *Soft Matter* **16**, 7503 (2020).
- [15] G. Miño, T. E. Mallouk, T. Darnige, M. Hoyos, J. Dauchet, J. Dunstan, R. Soto, Y. Wang, A. Rousselet, and E. Clement, *Physical Review Letters* **106**, 48102 (2011).
- [16] B. Wang, F. Ji, J. Yu, L. Yang, Q. Wang, and L. Zhang, *iScience* **19**, 760 (2019).
- [17] J. Orozco, B. Jurado-Sánchez, G. Wagner, W. Gao, R. Vazquez-Duhalt, S. Sattayasamitsathit, M. Galarnyk, A. Cortés, D. Sain-tillan, and J. Wang, *Langmuir* **30**, 5082 (2014).
- [18] M. R. Bailey, F. Grillo, N. D. Spencer, and L. Isa, *Advanced Functional Materials* **32**, 2109175 (2022).
- [19] M. R. Bailey, T. A. Gmür, F. Grillo, and L. Isa, *Chemistry of Materials* **35**, 3731–3741 (2023).
- [20] I. O. Götzke and G. Gompper, *Physical Review E* **82**, 041921 (2010).
- [21] A. Zöttl and H. Stark, *Annual Review of Condensed Matter Physics* **14**, 109 (2023).
- [22] R. Golestanian, *Physical Review Letters* **102**, 188305 (2009).
- [23] M. N. Popescu, S. Dietrich, M. Tasinkevych, and J. Ralston, *European Physical Journal E* **31**, 351 (2010).
- [24] K. K. Dey, F. Wong, A. Altemose, and A. Sen, *Current Opinion in Colloid and Interface Science* **21**, 4 (2016).
- [25] M. R. Bailey, N. Reichholf, A. Flechsig, F. Grillo, and L. Isa, *Particle and Particle Systems Characterization* **39**, 2100200 (2022).
- [26] M. R. Bailey, F. Grillo, and L. Isa, *Soft Matter* **18**, 7291–7300 (2022).
- [27] M. R. Bailey, C. M. B. Gutiérrez, J. Martín-Roca, V. Niggel, V. Carrasco-Fadanelli, I. Buttinoni, I. Pagonabarraga, L. Isa, and C. Valeriani, *arXiv* (2023), 10.48550/arXiv.2307.16193.
- [28] I. Theurkauff, C. Cottin-Bizonne, J. Palacci, C. Ybert, and L. Bocquet, *Physical Review Letters* **108**, 268303 (2012).
- [29] S. Thakur and R. Kapral, *Phys. Rev. E Stat. Nonlin. Soft Matter Phys.* **85**, 026121 (2012).
- [30] J. Palacci, S. Sacanna, A. P. Steinberg, D. J. Pine, and P. M. Chaikin, *Science* **339**, 936 (2013).
- [31] B. M. Mognetti, A. Šarić, S. Angioletti-Uberti, A. Cacciuto, C. Valeriani, and D. Frenkel, *Physical Review Letters* **111**, 245702 (2013).
- [32] B. Liebchen, D. Marenduzzo, and M. E. Cates, *Physical Review Letters* **118**, 268001 (2017).
- [33] F. Ginot, I. Theurkauff, F. Detcheverry, C. Ybert, and C. Cottin-Bizonne, *Nature Communications* **9**, 1 (2018).
- [34] X. Chen, X. Dong, A. Be'er, H. L. Swinney, and H. P. Zhang, *Physical Review Letters* **108**, 148101 (2012).
- [35] X. Chen, X. Yang, M. Yang, and H. P. Zhang, *EPL (Europhysics Letters)* **111**, 54002 (2015).
- [36] M. Theers, E. Westphal, K. Qi, R. G. Winkler, and G. Gompper, *Soft matter* **14**, 8590 (2018).
- [37] F. Mou, L. Kong, C. Chen, Z. Chen, L. Xu, and J. Guan, *Nanoscale* **8**, 4976 (2016).
- [38] L. Baraban, M. Tasinkevych, M. N. Popescu, S. Sanchez, S. Dietrich, and O. G. Schmidt, *Soft Matter* **8**, 48 (2012).
- [39] J. Palacci, S. Sacanna, A. Vatchinsky, P. M. Chaikin, and D. J. Pine, *Journal of the American Chemical Society* **135**, 15978 (2013).
- [40] F. Mou, J. Zhang, Z. Wu, S. Du, Z. Zhang, L. Xu, and J. Guan, *iScience* **19**, 415 (2019).
- [41] M. R. Bailey, A. R. Sprenger, F. Grillo, H. Löwen, and L. Isa, *Physical Review E* **106**, L052602 (2022).
- [42] M. A. Fernandez-Rodriguez, F. Grillo, L. Alvarez, M. Rathlef, I. Buttinoni, G. Volpe, and L. Isa, *Nature Communications* **11**, 1 (2020).
- [43] D. O. Pushkin and J. M. Yeomans, *Physical Review Letters* **111**, 1 (2013).
- [44] D. O. Pushkin, H. Shum, and J. M. Yeomans, *Journal of Fluid Mechanics* **726**, 5 (2013).
- [45] A. J. Mathijssen, R. Jeanneret, and M. Polin, *Physical Review Fluids* **3**, 033103 (2018).
- [46] R. Golestanian, T. B. Liverpool, and A. Ajdari, *New Journal of Physics* **9** (2007), 10.1088/1367-2630/9/5/126, arXiv:0701168 [cond-mat].
- [47] M. J. Lighthill, *Communications on Pure and Applied Mathematics* **5**, 109 (1952).
- [48] J. R. Blake, *Mathematical Proceedings of the Cambridge Philosophical Society* **70**, 303 (1971).
- [49] S. Michelin and E. Lauga, *Journal of fluid mechanics* **747**, 572 (2014).
- [50] M. N. Popescu, W. E. Uspal, Z. Eskandari, M. Tasinkevych, and S. Dietrich, *European Physical Journal E* **41**, 1 (2018).
- [51] J. Katuri, W. E. Uspal, M. N. Popescu, and S. Sánchez, *Science Advances* **7**, eabd0719 (2021).
- [52] A. I. Campbell, S. J. Ebbens, P. Illien, and R. Golestanian, *Nature Communications* **10**, 1 (2019).
- [53] M. Yang, A. Wysocki, and M. Ripoll, *Soft Matter* **10**, 6208 (2014).
- [54] I. P. Madden, L. Wang, J. Simmchen, and E. Luijten, *Small* **18**, 2107023 (2022).
- [55] P. J. Hoogerbrugge and J. M. Koelman, *Epl* **19**, 155 (1992).
- [56] P. Espanol and P. Warren, *Epl* **30**, 191 (1995).
- [57] E. M. Purcell, *American Journal of Physics* **45**, 3 (1977).

- [58] J. R. Howse, R. A. Jones, A. J. Ryan, T. Gough, R. Vafabakhsh, and R. Golestanian, *Physical Review Letters* **99**, 048102 (2007).
- [59] P. Kreissl, C. Holm, and J. De Graaf, *The Journal of Chemical Physics* **144** (2016).
- [60] A. Domínguez and M. N. Popescu, *Current Opinion in Colloid and Interface Science* **61**, 101610 (2022).
- [61] S. Friedlander, *AIChE Journal* **7**, 347 (1961).
- [62] P. M. Armenante and D. J. Kirwan, *Chemical Engineering Science* **44**, 2781 (1989).
- [63] T. M. Squires, R. J. Messinger, and S. R. Manalis, *Nature biotechnology* **26**, 417 (2008).
- [64] Q. Wang, F. Ji, S. Wang, and L. Zhang, *ChemNanoMat* **7**, 600 (2021).
- [65] J. Katuri, W. E. Uspal, J. Simmchen, A. Miguel-López, and S. Sánchez, *Science Advances* **4**, eaao1755 (2018).
- [66] P. Sharan, Z. Xiao, V. Mancuso, W. E. Uspal, and J. Simmchen, *ACS Nano*, 4599 (2022).
- [67] K. Qi, E. Westphal, G. Gompper, and R. G. Winkler, *Communications Physics* **5**, 49 (2022).
- [68] K. Xiong, J. Lin, Q. Chen, T. Gao, L. Xu, and J. Guan, *Matter* **6**, 1–18 (2023).
- [69] R. Mundaca-Urbe, M. Holay, A. Abbas, N. Askarinam, J. S. Sage-Sepulveda, L. Kubiawicz, R. H. Fang, L. Zhang, and J. Wang, *ACS Nano* **17**, 9272 (2023).
- [70] P. Thörnig, *Journal of large-scale research facilities JLSRF* **7**, A182 (2021).
- [71] D. A. Fedosov, B. Caswell, and G. E. Karniadakis, *Biophys. J.* **98**, 2215 (2010).
- [72] W. Helfrich, *Z. Naturforsch.* **28**, 693 (1973).
- [73] F. Alarcón, C. Valeriani, and I. Pagonabarraga, *Soft Matter* **13**, 814 (2017).
- [74] D. P. Singh, U. Choudhury, P. Fischer, and A. G. Mark, *Advanced Materials* **29**, 1701328 (2017).
- [75] E. Kepten, I. Bronshtein, and Y. Garini, *Physical Review E - Statistical, Nonlinear, and Soft Matter Physics* **87**, 1 (2013), arXiv:1212.0793.
- [76] M. R. Bailey, A. R. Sprenger, F. Grillo, H. Löwen, and L. Isa, *Physical Review E* **106** (2022), 10.1103/physreve.106.1052602.
- [77] R. Cerbino and V. Trappe, *Physical Review Letters* **100** (2008), 10.1103/physrevlett.100.188102.

THE SUPPORTING INFORMATION INCLUDES:

Text S1: Materials and Methods

Fig. S1: Definition of clustering and the different velocity distributions

Fig. S2: Influence of actively transported tracers on ensemble averaged values

Fig. S3: Fitting the lag-time at which the maximal kurtosis for the distribution of displacements of tracers is observed

Fig. S4: Distribution of tracer displacements in the presence of non-swimming microswimmers (UV light off)

Figure S5: Evidence for phoretic interactions between the Janus particles (pumps) and passive nanoparticle tracers

Figure S6: Influence of Janus pumps on nanoparticle tracer dynamics in the near- and far-field

Figure S7: Lack of mixing effect observed for nanoparticle tracers in a microswimmer bath

Figure S8: Comparison of different approaches to evaluate nanoparticle tracer dynamics to evaluate their accuracies

Materials and Methods

Experimental setup and materials. Particles were imaged on an inverted microscope (Nikon Eclipse Ti2e) under Köhler illumination with white light using a 40× objective (CFI S Plan Fluor ELWD 40XC) with adjustable collar (set to 1 mm) unless otherwise specified. Due to a density mismatch, the particles sediment to the glass substrate, where they remain under the experimental conditions used. Images were acquired at 50 FPS using a Hamamatsu C14440-20UP digital camera. The Janus microswimmers were activated with a UV LED (365 nm, Prizmatix UHP-F-365), at a power density of 44 mW/mm², in the presence of a chemical fuel (H₂O₂ 3 % v/v, Acros Organics). The tracer particles (230 nm and 1700 nm diameter, microParticle GmbH) were fluorescent under illumination with the UV LED source, and did not require an additional excitation source (Ex/Em 502/518 nm). To ensure a near-constant number density (area fraction Φ) of studied microswimmers, it was necessary to create a confined system to prevent their escape to non-illuminated regimes. This was achieved by creating wells (diameter = 250 μ m) in glass slides by HF etching. To avoid boundary effects, only the region bounded by a box (83.2 x 83.2 μ m) centred in this well was studied. The cells were sealed using an upper glass slide and PDMS spacer to prevent convective drift.

The expression for $\hat{\tau}_c$ was derived as follows: Assuming that N ballistic swimmers (ignoring diffusion) will explore an area given by:

$$\langle \Delta \mathbf{r}^2(\tau) \rangle \sim N_p v_0^2 \tau^2. \quad (1)$$

then it follows that they will travel a distance l_N in $\tau = l_N / (v_0 \sqrt{N_p})$ seconds.

Likewise, assuming N_t equidistantly spaced tracers in the system area A , we approximate the mean inter-tracer distance to be $\langle l_t \rangle = \sqrt{A} / \sqrt{N_t}$. Therefore, the average predicted time $\hat{\tau}_c$ for N ballistic swimmers to travel the mean inter-tracer distance can be obtained by equating l_N with $\langle l_t \rangle$, giving the following collision time between swimmers and tracers:

$$\hat{\tau}_c \sim \frac{\sqrt{A_T}}{v_0 \sqrt{N_p N_{trac}}} \quad (2)$$

Modeling fluid flow in simulations. Fluid flow is modeled by the dissipative particle dynamics (DPD) method [55, 56], which is a mesoscopic hydrodynamics simulation technique. In DPD, fluid is represented by a collection of N_s solvent particles. DPD particle interactions are pairwise and soft, while particle velocities \mathbf{v}_i and positions \mathbf{r}_i follow the Newton's second law of motion

$$\begin{aligned} \frac{d\mathbf{r}_i}{dt} &= \mathbf{v}_i, \\ \frac{d\mathbf{v}_i}{dt} &= \frac{1}{m_i} \sum_{j \neq i} (\mathbf{F}_{ij}^C + \mathbf{F}_{ij}^D + \mathbf{F}_{ij}^R), \end{aligned} \quad (3)$$

where m_i is the particle mass and the forces \mathbf{F}_{ij}^C , \mathbf{F}_{ij}^D , and \mathbf{F}_{ij}^R define conservative, dissipative, and random interactions, respectively. The above equations of motion are integrated using the velocity-Verlet algorithm. The total force exerted on a particle i by particle j is given by

$$\begin{aligned} \mathbf{F}_{ij}^C &= b \left(1 - \frac{r_{ij}}{r_c} \right) \hat{\mathbf{r}}_{ij}, \\ \mathbf{F}_{ij}^D &= -\gamma \omega^D(r_{ij}) (\mathbf{v}_{ij} \cdot \hat{\mathbf{r}}_{ij}) \hat{\mathbf{r}}_{ij}, \\ \mathbf{F}_{ij}^R &= \sigma_{dpd} \omega^R(r_{ij}) \frac{\xi_{ij}}{\sqrt{dt}} \hat{\mathbf{r}}_{ij}, \end{aligned} \quad (4)$$

where $\mathbf{r}_{ij} = \mathbf{r}_i - \mathbf{r}_j$, $\hat{\mathbf{r}}_{ij} = \mathbf{r}_{ij} / r_{ij}$, and $\mathbf{v}_{ij} = \mathbf{v}_i - \mathbf{v}_j$. The coefficients b , γ , and σ_{dpd} determine the strength of conservative, dissipative, and random forces, respectively. ω^D and ω^R are weight functions and ξ_{ij} is a symmetric normally-distributed random variable with zero mean and unit variance. All forces act within a sphere of cutoff radius r_c . The random and dissipative forces form a thermostat and have to satisfy the fluctuation-dissipation theorem [56] to maintain the equilibrium temperature T in DPD system. This results in two conditions,

$$\omega^D(r_{ij}) = [\omega^R(r_{ij})]^2, \quad \sigma_{dpd}^2 = 2\gamma k_B T. \quad (5)$$

The typical choice for the weight function is $\omega^R(r_{ij}) = (1 - r_{ij}/r_c)^s$, where s is a selected exponent.

Rigid walls are simulated by immobilized DPD particles having identical number density and interactions as the fluid particles. The immobile wall particles enforce no-slip boundary conditions (BCs) at the walls through dissipative interactions with the fluid particles. In order to prevent wall penetration by fluid particles, reflective surfaces are introduced at the interface between the fluid and the walls. Slip BCs at the walls can be modeled by turning off the dissipative interactions between fluid and wall particles.

Model of active particles and passive tracers in simulations. Both active swimmers and passive tracers are represented by an arrangement of particles uniformly distributed on a spherical surface and forming a triangulated network (i.e. membrane model). To ensure the structural integrity of the triangulated network, it is supplied with shear elasticity, bending rigidity, and constraints related to the surface area and enclosed volume [71]. The bonds connecting adjacent vertices within the network provide shear elasticity defined by a potential function $U_e = U_{wlc} + U_{pow}$ as [71].

$$U_{wlc} = \frac{k_B T l_m}{4p} \frac{3x^2 - 2x^3}{1-x}, \quad U_{pow} = \frac{k_p}{l}, \quad (6)$$

where l is the spring length, l_m is the maximum spring extension, $x = l/l_m$, p is the persistence length, and k_p is the repulsive force coefficient. The bending rigidity is described by the Helfrich bending energy [72]

$$U_b = \frac{\kappa}{2} \sum_i \sigma_i (H_i - H_0^i)^2, \quad (7)$$

where κ is the bending rigidity, $H_i = \mathbf{n}_i \cdot \sum_{j(i)} \sigma_{ij} \mathbf{r}_{ij} / (\sigma_i r_{ij})$ is the discretized mean curvature at vertex i , \mathbf{n}_i is the unit normal at the membrane vertex i , $\sigma_i = \sum_{j(i)} \sigma_{ij} r_{ij} / 4$ is the area corresponding to vertex i (the area of the dual cell), $j(i)$ corresponds to all vertices linked to vertex i , and $\sigma_{ij} = r_{ij} (\cot \theta_1 + \cot \theta_2) / 2$ is the length of the bond in the dual lattice, where θ_1 and θ_2 are the angles at the two vertices opposite to the edge ij in the dihedral. Finally, H_0^i is the spontaneous curvature at vertex i .

The area and volume conservation constraints are given by [71]

$$U_a = \frac{k_a (A - A_0^{tot})^2}{2A_0^{tot}} + \sum_{m \in 1 \dots N_t} \frac{k_d (A_m - A_0^m)^2}{2A_0^m}, \quad (8)$$

$$U_v = \frac{k_v (V - V_0^{tot})^2}{2V_0^{tot}}, \quad (9)$$

where A is the current area of the membrane, A_0^{tot} is the targeted global area, A_m is the area of the m -th triangle from N_t triangles on the triangulated surface, A_0^m is the targeted area of the m -th triangle determined by the triangular mesh on the particle surface, V is the instantaneous membrane volume, and V_0^{tot} is the targeted volume. Furthermore, k_a , k_d , and k_v are the global area, local area and volume constraint coefficients, respectively.

Both swimmers and tracers are submerged within a DPD fluid, and also filled by fluid DPD particles due to their membrane-like representation. The membrane surfaces of all suspended active particles and tracers serve as a boundary separating DPD particles inside and outside of the membranes. This is achieved through the reflection of solvent particles at the membrane surfaces from inside and outside. Note that the dissipative and random forces between the internal and external fluid particles are deactivated, and only the conservative force is employed to maintain uniform fluid pressure across the membranes. No slip BCs between the fluid and suspended colloidal particles are implemented through the proper adjustment of the friction coefficient γ between fluid and membrane particles [71].

Propulsion of active swimmers is realized through a slip velocity at their surface using the spherical squirmer model [73]

$$\mathbf{u}_s = (B_1 \sin(\phi) + B_2 \sin(\phi) \cos(\phi)) \mathbf{t}_\phi, \quad (10)$$

where \mathbf{t}_ϕ represents the local tangential vector in the ϕ direction at the swimmer surface, and ϕ corresponds to the angle between the orientation of the squirmer and the vector extending from its center of mass to a local position on its surface. The coefficient B_1 governs the propulsion strength of the squirmer, while B_2 introduces a front-back asymmetry into the slip-velocity field. In bulk, the spherical squirmer swims with a velocity $v_0 = 2B_1/3$. We employ the dimensionless ratio $\beta = \frac{B_2}{B_1}$ to characterize the mode of propulsion, where $\beta < 0$ represents a pusher, $\beta = 0$ corresponds to a neutral swimmer, and $\beta > 0$ models a puller. To enforce the slip velocity at the squirmer surface, the dissipative interaction between the squirmer particles and those of the surrounding fluid is adjusted as follows

$$\mathbf{F}_{ij}^D = -\gamma \omega^D (r_{ij}) (\hat{\mathbf{r}}_{ij} \cdot \mathbf{v}_{ij}^*) \hat{\mathbf{r}}_{ij}, \quad \mathbf{v}_{ij}^* = \mathbf{v}_i - \mathbf{v}_j + \mathbf{u}_s^i, \quad (11)$$

where \mathbf{u}_s^i is the slip velocity at the position of squirmer particle i , while j corresponds to an outer-fluid DPD particle.

Excluded volume interactions between active squirmers and tracers are imposed through the 12-6 Lennard-Jones (LJ) potential as

$$U_{LJ}(r) = 4\epsilon \left[\left(\frac{\sigma_{LJ}}{r} \right)^{12} - \left(\frac{\sigma_{LJ}}{r} \right)^6 \right], \quad (12)$$

where σ_{LJ} is the distance at which $U_{LJ}(\sigma_{LJ}) = 0$ and ϵ is the potential strength. Note that only the repulsive part of the LJ potential is employed by setting the cutoff radius to $r_c^{LJ} = 2^{1/6}\sigma_{LJ}$.

Simulation setup and parameters. The simulation domain corresponds to a slit-like geometry with a size of $100r_c \times 100r_c \times 22r_c$ and periodic BCs in the xy plane. In the z axis, the fluid layer of thickness $20r_c$ is confined between two walls, each with a thickness of r_c . The fluid modeled by a collection of DPD particles has a number density of $n = 5/r_c^3$ ($r_c = 1.0$ is selected in simulations). The DPD force coefficients for interactions between fluid particles are $b = 50k_B T/r_c$, $\gamma = 14.15\sqrt{mk_B T}/r_c$, and $s = 0.15$, where $m = 1$ is the particle mass and $k_B T = 2$ is the unit of energy. These parameters lead to a fluid dynamic viscosity of $\eta = 16.7\sqrt{mk_B T}/r_c^2$.

Suspended squirmers are constructed from 1000 particles placed on a spherical surface with a diameter $d_{Sq} = 6.4r_c$. The largest investigated tracers have the same diameter. The area fraction of $\Phi = 0.05$ corresponds to 18 simulated squirmers, to which 10 tracers were added. Both the squirmers and tracers are placed at the lower wall ($z = 0$) with no-slip BCs, and restricted to a fluid layer of thickness $7.3r_c$, in order to properly capture the quasi-2D environment in experiments. At the upper wall ($z = 20r_c$) slip BCs are imposed, which partially accounts for a larger domain in experiments. Coupling between the squirmer/tracer particles and fluid particles assumes $b = 0$ and $\gamma = 12\sqrt{mk_B T}/r_c$ with $s = 0.1$ and $r'_c = 0.7r_c$. The value of γ here is computed such that the imposed slip BCs at the squirmer surface are obtained [71]. The time step in simulations is $\Delta t = 0.007r_c\sqrt{m/k_B T}$.

To relate simulation and physical units, we introduce characteristic length and time scales. The length scale is based on the squirmer diameter $d_{Sq} = 6.4r_c$, resulting in r_c to represent approximately $0.34 \mu m$ ($d_S = 2.16 \mu m$ in experiments). Therefore, the simulation domain corresponds to $34 \times 34 \times 6.8 \mu m$. The time scale is $\tau = d_{Sq}/v_M$, where v_M is the modal velocity of the velocity distribution of active particles in the xy plane, see Fig. 1(b) in the main text.

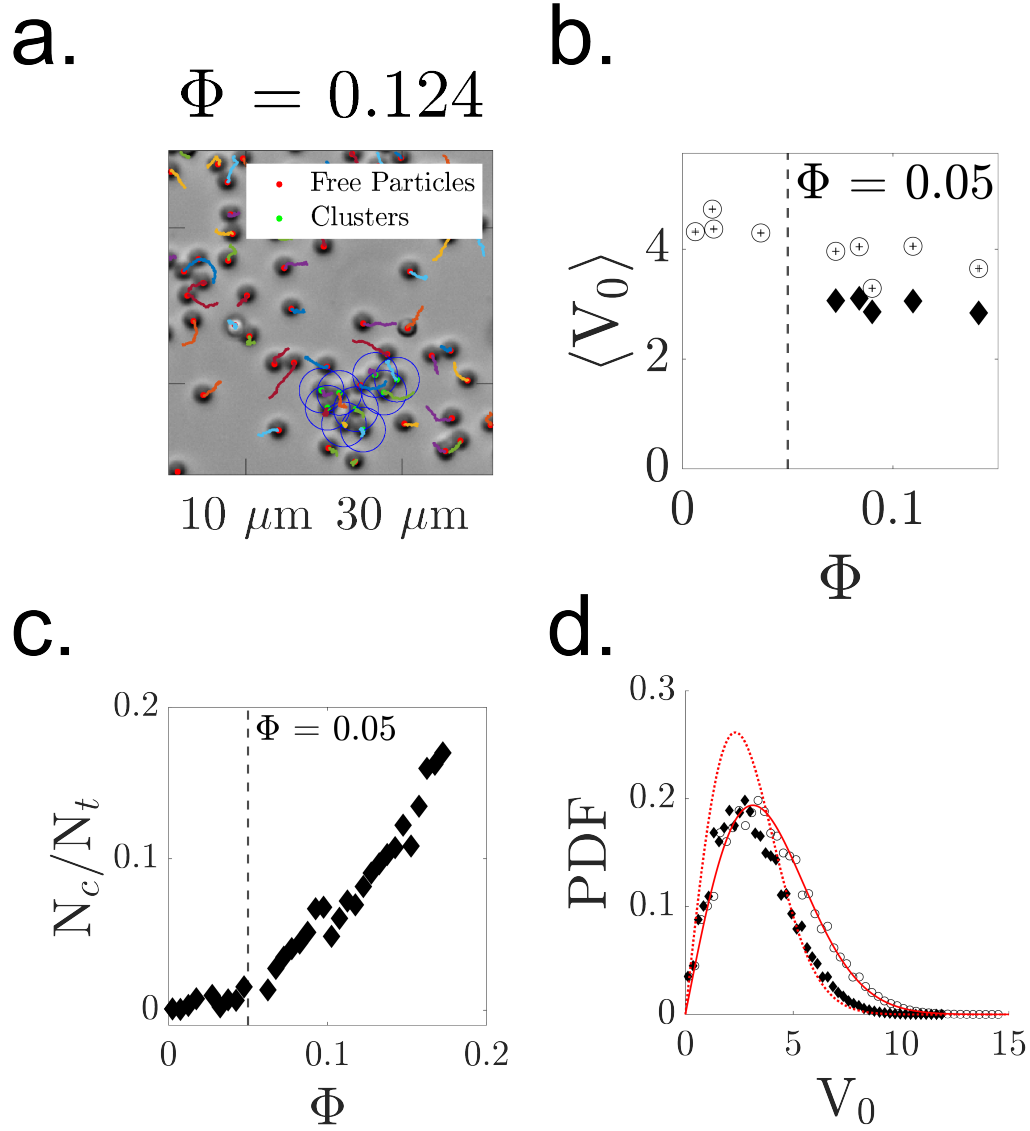


Figure. S 1. Separating “clustered” particles from “free” particles. a. Identification of “clustered” particles from micrographs. Clusters are defined as particles with 2 or more nearest neighbours within $2.5R$ for at least 12 frames (0.24 s, [28]). b. Mean velocity of free (open circle) and clustered (closed diamond) microswimmers. c. Onset of clustering at an area fraction $\Phi \sim 0.05$. d. Instantaneous velocity distributions of free and clustered particles (symbols as before). The red curves (solid and dashed for the free and clustered particles respectively) show the best fits of the Maxwell distribution [8]. We clearly see that clustered particles cannot be well explained by this distribution, while the motion of the non-interacting microswimmers is well captured. Notably, the distribution of velocities follows that for neutral squirmers (see main text, Figure 4).

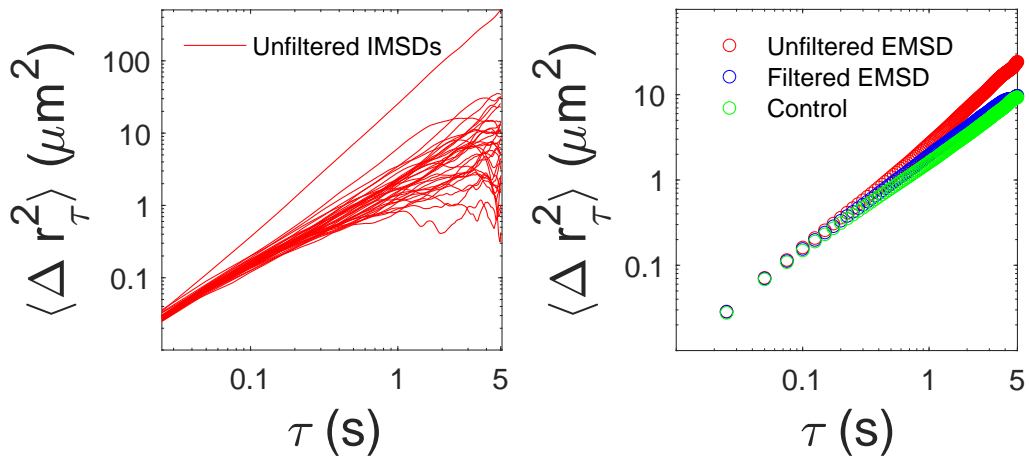


Figure. S 2. Effect of “actively transported” colloids on the ensemble-mean-squared-displacement (EMSD) of all tracers. Left: The individual MSDs (IMSDs) of multiple tracer particles (here, $1\mu\text{m}$) in a dilute suspension of synthetic microswimmers. We see one extreme outlier, which corresponds to a singular tracer particle being actively transported by a microswimmer (via phoretic attraction). Right: The single actively transported tracer significantly contributes to the overall EMSD (red - due to averaging of all values). Removing this single IMSD from the ensemble (blue) collapses the EMSD of the tracers onto the control EMSD (green) of passive tracers in the absence of active microswimmers. This highlights the issues of blindly using averaged values alone when evaluating systems with large outliers.

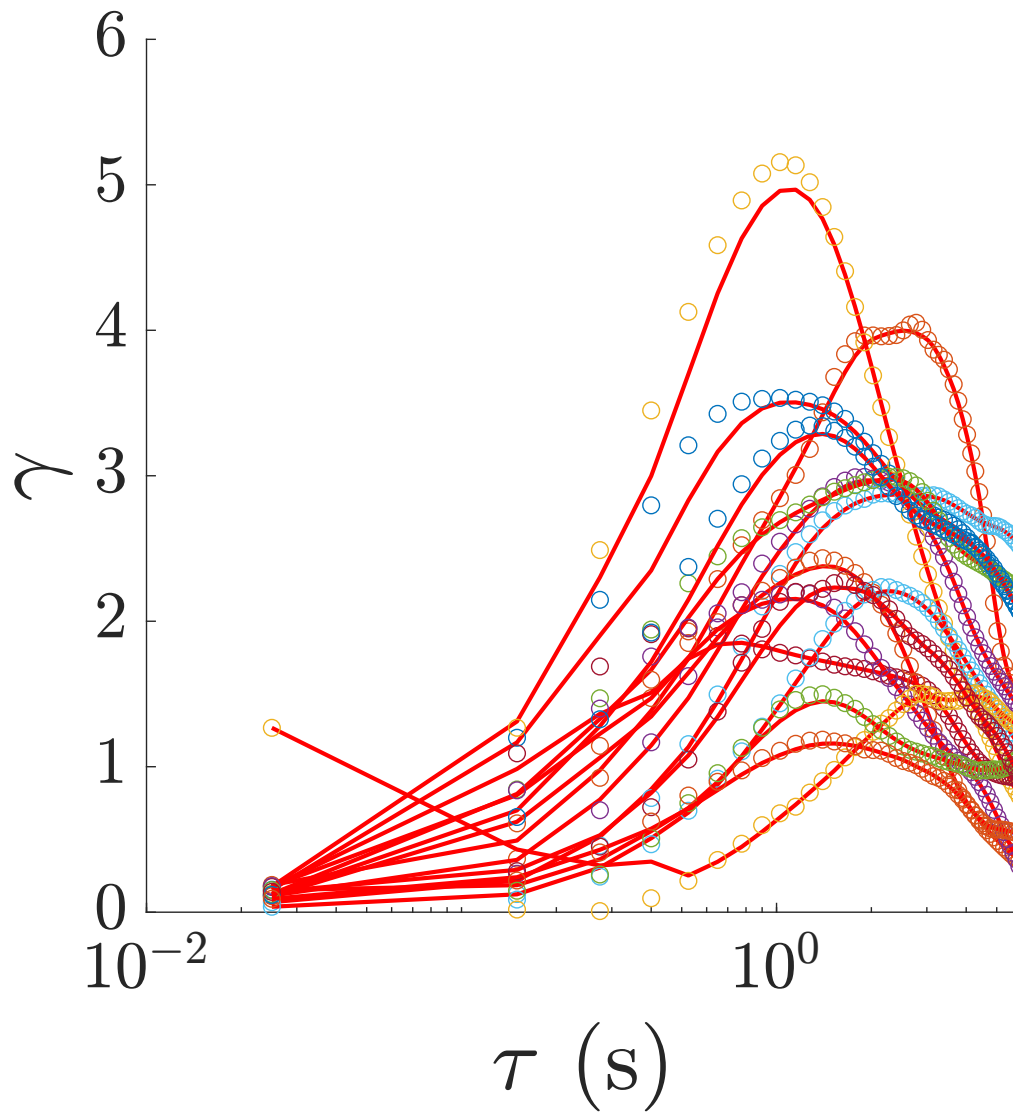


Figure. S 3. Extracting the experimental $\tau_{\gamma=\text{argmax}_{\tau}(\gamma)}$ from experiments performed under different conditions (see Figure 2 b. of the main text). $\gamma(\tau)$ is extracted from the displacements of the tracers in different experiments (varying tracer and swimmer concentration), and a smoothing spline is then fitted to extract τ at which the value of γ is maximised [42].

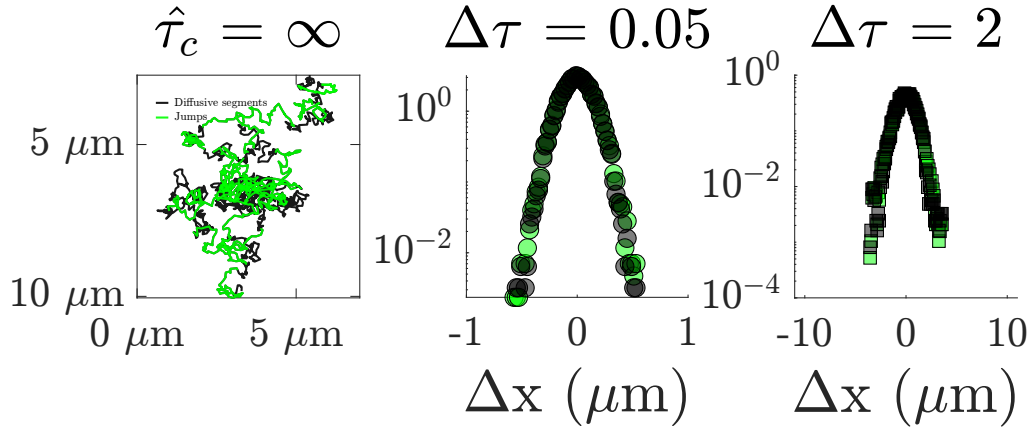


Figure. S 4. Tracer displacements in the presence of microswimmers which are passively diffusing (no UV illumination). At both short and long lag times $\Delta\tau$, the distribution is Gaussian. Contrast this to the enhanced diffusivity of tracers in the presence of motile microswimmers, shown in Figure 3 (top row) of the main text. Note that the autocorrelation approach to extracting jumps also identifies jumps in the passive case, but that the resulting distributions are unaffected.

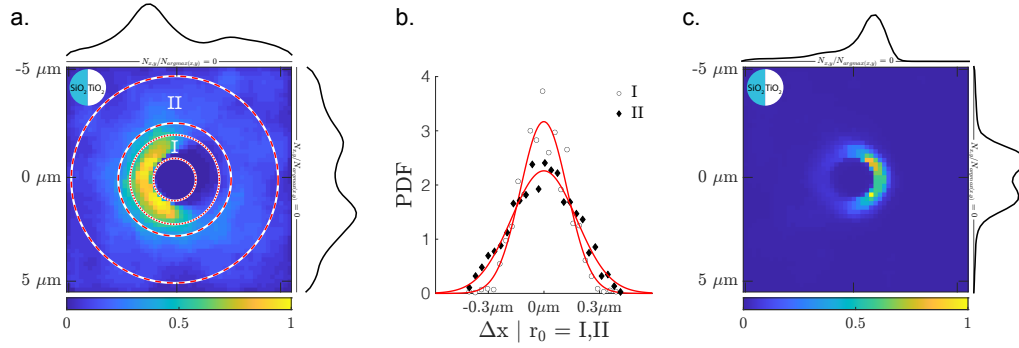


Figure. S 5. Demonstration of the phoretic interactions between the Janus microswimmers and the PS tracer nanoparticles. By immobilizing our microswimmers and modulating the pH, we also observe a phoretic contribution to the generated flow fields, in agreement with previous reports for TiO_2 - SiO_2 systems [74]. The values are averaged over at least 4 Janus pumps (stuck to the substrate via drying) in each case. Specifically, we note the change in the accumulation of the tracer nanoparticles as tetramethylammonium hydroxide (TMAH) is added to modulate the pH, following [74]. a. Accumulation of PS nano-tracers around a fixed Janus particle at the SiO_2 hemisphere under standard experimental conditions in the presence of H_2O_2 with UV illumination ($\text{pH} \sim 4$, orientation shown in inset, top left). Colour coding indicates the normalised number density, as well as the averaged profiles in X and Y. b. Distribution of displacements of the nanoparticle tracers in the regions marked I and II in a. We see that near the Janus particle, tracer displacements decrease due to accumulation. Far from the particle, we observe the expected Gaussian distribution (also see Figure S5). c. Accumulation of PS nano-tracers around a fixed Janus particle at the TiO_2 hemisphere under modulation of the pH ($\text{pH} \sim 7$) via addition of TMAH, in the presence of H_2O_2 with UV illumination (orientation shown in inset, top left). For these experiments, tracers were visualised using a 100x oil objective.

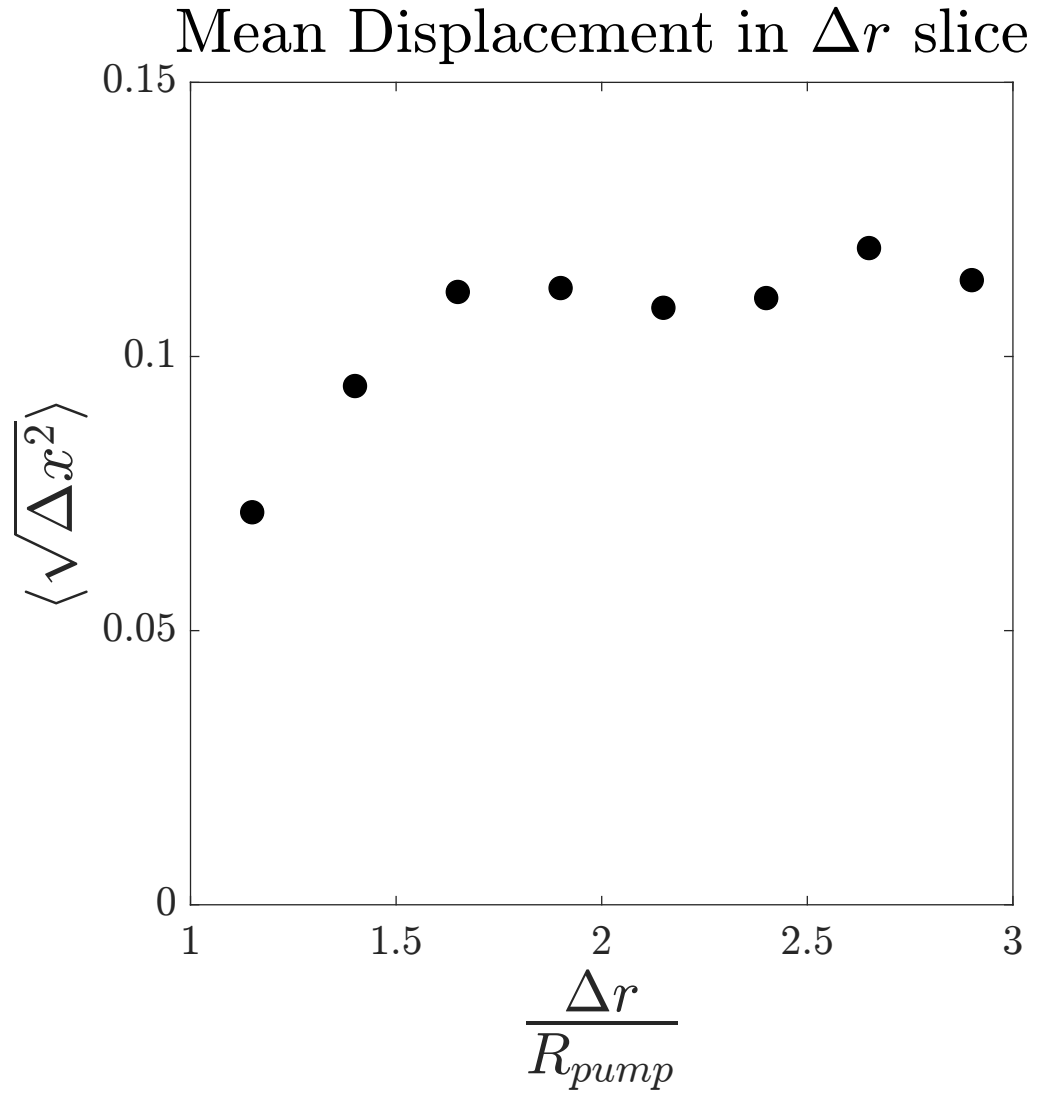


Figure. S 6. Average instantaneous displacement of tracer nanoparticles in rings evaluated around the Janus pumps evaluated in Figure S4 a. We see that outside of the inner rings (where the tracers accumulate due to phoretic interactions), the average displacements of the tracers rapidly saturate, indicating little-to-no effect of the hydrodynamic flows created by the microswimmer on tracers at a distance.

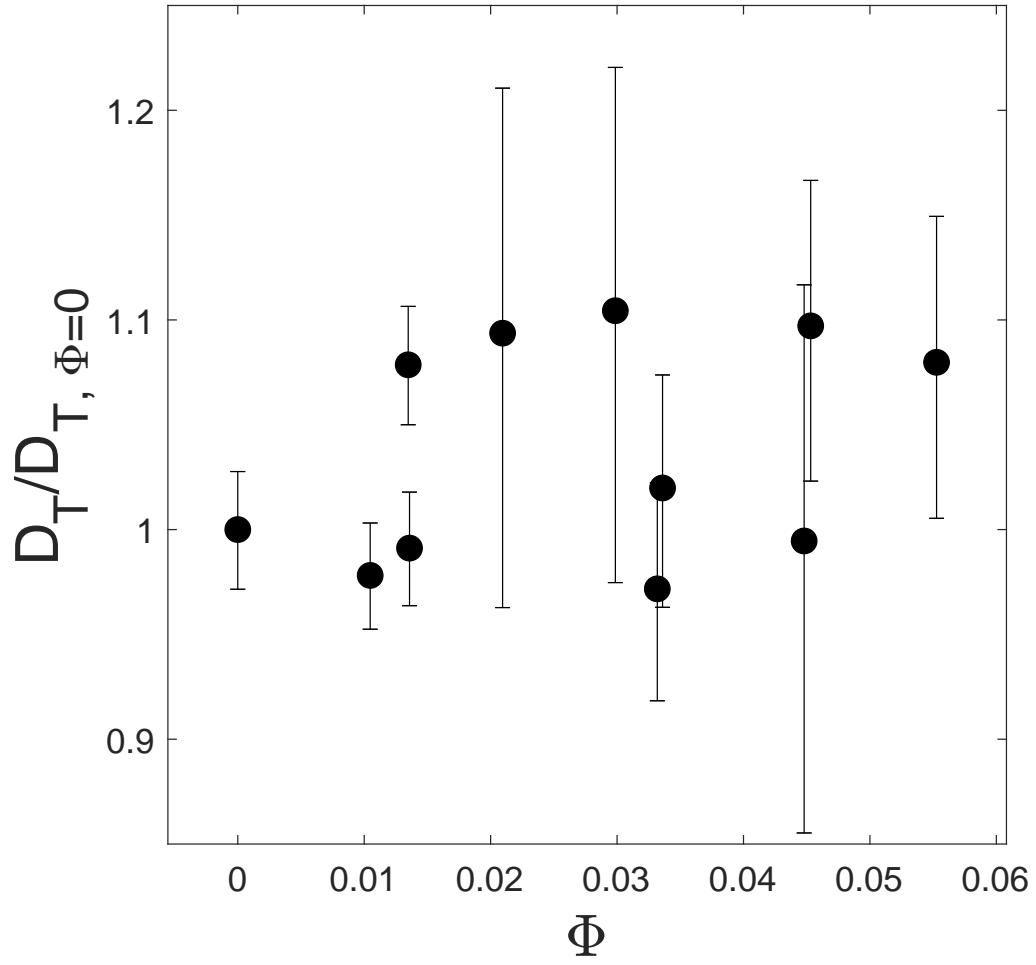


Figure. S 7. Fitted translational diffusion coefficients D_T of tracer nanoparticles in the presence of different concentrations (represented by area fraction, Φ) of microswimmers, normalised by the control at $\Phi = 0$. The mean value and error bars are obtained from the distribution of D_T fitted from the mean logarithmic squared displacement [75, 76] (MLSD, given by $MLSD = \log(4D_T) + \alpha \log(\tau)$), assuming a log-normal distribution (also see Figure S7 c.). We see that there is no clear trend in the values of D_T with the presence of microswimmers, indicating the lack of an enhancement in their diffusivity (via mixing), which we attribute to their high initial diffusion coefficient (arising from their small size).

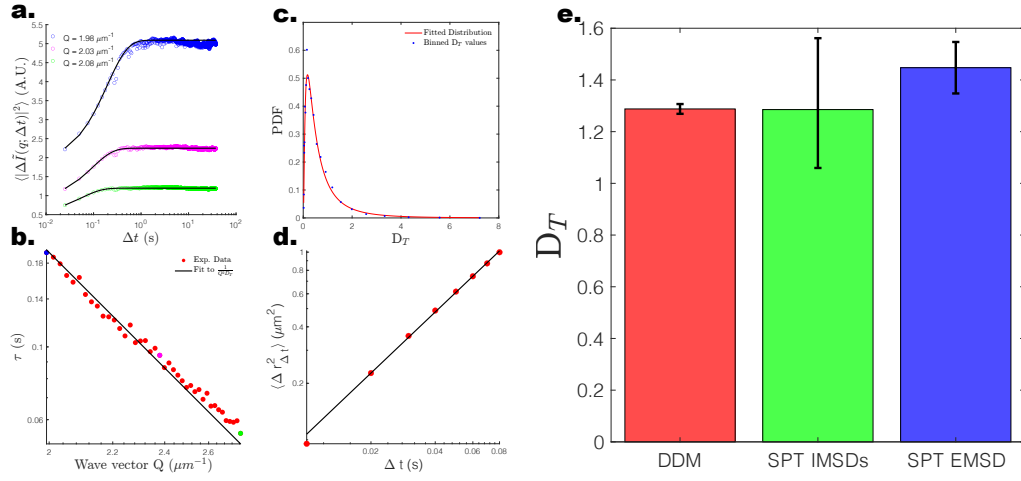


Figure. S 8. Comparison of the fitting approaches used to extract D_T values of the (control, i.e. in the absence of microswimmers) PS nanoparticle tracers, to confirm the accuracy of various approaches. a-b. Fitting of D_T via differential dynamic microscopy (DDM [77]). c. Fitting a log-normal distribution to the binned values of D_T obtained using the MLSD of individual tracers (also see Figure S6) d. Fitting the EMSD of the tracers directly. e. Comparison of the fits obtained using different approaches (in $\mu\text{m}^2 \text{s}^{-1}$). We see good agreement between using DDM and the distribution of the MLSDs of individual nanoparticle tracers in the passive case. As the presence of microswimmers (additional scattering sources) affects the interpretation of DDM results, we therefore use the values obtained from the distribution of the IMSDs.